International Journal of Solids and Structures 47 (2010) 2246–2259

Contents lists available at ScienceDirect

International Journal of Solids and Structures

journal homepage: www.elsevier.com/locate/ijsolstr

Effects of the dynamic wheel–rail interaction on the ground vibration generated by a moving train

Yuanqiang Cai [a,b,*], Zhigang Cao [a], Honglei Sun [a], Changjie Xu [a]

[a] MOE Key Laboratory of Soft Soils and Geoenvironmental Engineering, Zhejiang University, Hangzhou 310027, PR China
[b] College of Architecture and Civil Engineering, Wenzhou University, Wenzhou 325035, PR China

ARTICLE INFO

Article history:
Received 6 August 2009
Received in revised form 28 March 2010
Available online 19 April 2010

Keywords:
Poroelasticity
Moving train
Rail irregularity
Fourier transform

ABSTRACT

Based on Biot's fully dynamic poroelastic theory, the dynamic responses of the poroelastic half-space soil medium due to quasi-static and dynamic loads from a moving train are investigated semi-analytically. The dynamic loads are assumed to be generated from the rail surface irregularities. The vehicle dynamics model is used to simulate the axle loads (quasi-static loads) and the dynamic loads from a moving train. The compatibility of the displacements at wheel–rail contact points couple the vehicle and the track–ground subsystem, and yield equations for the dynamic wheel–rail loads. A linearized Hertzian contact spring between the wheel and rail is introduced to calculate the dynamic loads. Using the Fourier transform, the governing equations for the poroelastic half-space are then solved in the frequency–wavenumber domain. The time domain responses are evaluated by the fast inverse Fourier transform. Numerical results show that the dynamic loads can make important contribution to dynamic response of the poroelastic half-space for different train speed, and the dynamically induced responses lie in a higher frequency range. The ground vibrations caused by the moving train can be intensified as the primary suspension stiffness of the vehicle increases.

1. Introduction

The ground vibrations caused by moving trains have been intensified as the trains run faster. Thus, there is a strong desire to predict the train-induced ground vibration accurately as it can disturb the living of inhabitants along the line. More and more numerical models have been proposed for the prediction of the train-induced ground vibration.

Krylov (1995) proposed a model to investigate the dynamic responses of the track generated by a superfast train. The ground was treated as an elastic half-space, and an approximate expression for Green's function of the elastic soil medium was used, by taking the Rayleigh-wave's contribution into account only. Kargarnovin and Younesian (2004), Kargarnovin et al. (2005) investigated the Timshenko beam vibration generated by moving loads on the Pasternak visco-elastic half space and nonlinear visco-elastic half space successively. Using a sandwich beam-structure track model consist of rail tracks, continuous sleepers and the ballast, Picoux and Le Houédec (2005) and Sheng and Jones (1999) studied the ground vibration generated by train loads. The soil medium was modeled as a layered elastic half-space. Vostroukhov and Metrikine (2003) and Takemiya and Bian (2005) studied the dynamic response of a rail beam on a visco-elastic half-space, and the effects of the discrete masses of sleepers on the dynamic response were investigated. In these works, the train loads were generally treated as a series of constant loads (axle loads). However, during the operation of the train, the dynamic loads may be caused by irregularities, such as wheel flats, rail surface irregularities and wheel eccentricity. Several researchers (Knothe and Grassie, 1993; Zai and Cai, 1997; Zai et al., 1994; Sheng et al., 2004, 2003) extended the above works by considering the dynamic loads caused by the rail irregularities. A Hertzian contact spring was introduced between the wheelset and rail. It was obtained that the dynamic loads played an important role for the train-induced ground vibration and should be taken into consideration in the study of train-induced ground vibration. Metrikine et al. (2005) studied the stability of a moving train bogie on the track, and the bogie was modeled as a two-degree-of freedom system. Recently, Lombaert and Degrand (2009) and Katou et al. (2008) studied the ground vibration caused by both the quasi-static and dynamic loads at a subcritical train speed by numerical method. The numerical results were verified by the in situ experiments, and it was obtained that the free-field vibration response was dominated by the contribution of dynamic load. For all the works above, the soil was treated as an elastic or visco-elastic medium. However, as there is under-ground water in the considered soil medium, which affects the wave propagation

* Corresponding author at: College of Architecture and Civil Engineering, Wenzhou University, Wenzhou 325035, PR China. Tel./fax: +86 571 8820 8774.
E-mail address: caiyq@zju.edu.cn (Y. Cai).

0020-7683/$ - see front matter © 2010 Elsevier Ltd. All rights reserved.
doi:10.1016/j.ijsolstr.2010.04.013

apparently, the fully saturated poroelastic soil model is closer to the actual situation.

Biot (1956, 1962) pioneered the development of an elastodynamic theory for a fluid-filled elastic porous medium. Later, many researchers applied Biot's theory to deal with dynamic responses of a fully saturated soil under moving load (Burke and Kingsbury, 1984; Siddharthan et al., 1993; Theodorakopoulos, 2003; Theodorakopoulos et al., 2004; Jin, 2004; Lu and Jeng, 2007). Applying Biot's theory, Cai et al. (2008, 2009) studied the dynamic responses of the track–ground system subjected to the train loads using a sandwich beam-structure track model. The effects of the characteristics of poroelastic soil medium on the dynamic responses were studied in detail. It was found that the dynamic characteristics of the poroelastic soil medium were quite different from that of the elastic soil medium when the train speed exceeded the critical speed of the track–ground system. The major limitation in these works is that the dynamic wheel–rail force was not considered in these investigations.

In consideration of the two aspects above, a more realistic vehicle–track-poroelastic half-space coupling model is needed to investigate the ground vibration caused by moving trains. On the other hand, some researchers (Chai and Miura, 2002) focused their study on the permanent deformation of the subsoil, which is an important factor controlling the service life as well as the maintenance cost of the railway lines, due to train load using an elastic soil model. However, it is well known that the deformation of subsoil is caused by the effective stress in the poroelastic soil medium. Thus, it is desirable to calculate the effective stress in subsoil using a poroelastic soil model in consideration of the dynamic wheel–rail force.

In this paper, a vehicle–track–ground coupling model, consisting of vehicles, a track and a poroelastic half-space, is proposed for the study of train-induced ground vibration. The dynamic wheel–rail forces are considered by introducing a Hertizian contact spring between each wheelset and the rail. The vehicles and track–ground subsystem are coupled by the displacement compatibility at wheel–rail contact points. Biot's dynamic poroelastic theory is used to characterize the poroelastic half-space soil medium considering the coupling of soil particles and pore water of the soil medium. Using the double Fourier transform, the governing equations of the track–ground system are solved analytically in the frequency–wavenumber domain. The time-domain results are obtained by the fast inverse Fourier transform. The quasi-statically induced and dynamically induced displacements, pore water pressures and effective stresses (caused by the axle load and dynamic load, respectively) are calculated for train speeds below and above the Rayleigh-wave speed of the half-space. The effects of the primary suspension stiffness of the vehicle and the soil permeability on the quasi-statically and dynamically induced responses are investigated. Furthermore, the different frequency components of the quasi-statically and dynamically induced responses are investigated.

2. Governing equations of the vehicle and track–ground system

2.1. Receptances of the track–ground system at the wheel–rail contact points

The receptance herein denotes the displacement amplitude of the rail at the wheel–rail contact point due to a unit vertical harmonic load with exciting frequencyΩ. The vehicle–track–ground coupling system is shown in Fig. 1a, and the Hertizian contact spring between the wheel and rail is shown in Fig. 1b.

The track model of Sheng and Jones (1999) is introduced in this paper. The rails, sleepers and ballast are modeled as an infinite

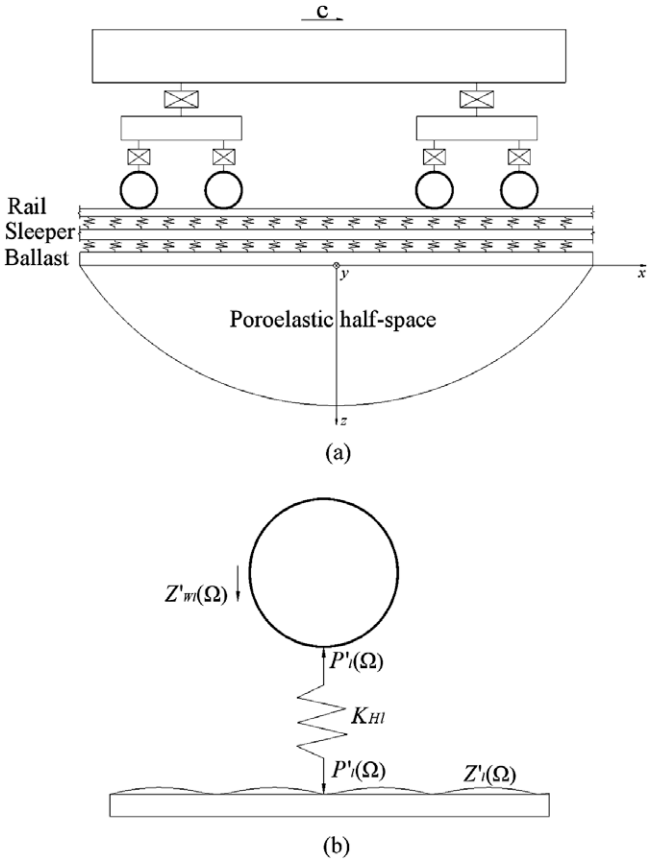

Fig. 1. The model of vehicle–track–ground coupling system: (a) the vehicle–track–ground system, and (b) the Hertzian contact spring between the wheelset and the rail.

Euler beam, continuous mass and Cosserat model, respectively. In order to calculate the receptance of the track–ground system, a unit vertical harmonic load $e^{i\Omega t}$ is applied on the rail, which is pointing downwards and located at $x = 0$ when $t = 0$. The load moves along the rails at speed c. The governing equation for a rail represented by an Euler beam is written as:

$$EI\frac{\partial^4 u_R(x,t)}{\partial x^4} + m_R\frac{\partial^2 u_R}{\partial t^2} + k_P[u_R(x,t) - u_S(x,t)] = e^{i\Omega t}\delta(x - ct) \quad (1)$$

in which u_R is the vertical displacement of the Euler Beam, EI is the bending stiffness of the rail beam, m_R is the mass of the rail per unit length, k_P denotes the spring constant of the rail pads, and u_S is the vertical displacement of the sleepers.

A continuous mass model is used for the sleepers:

$$m_S\frac{\partial^2 u_S(x,t)}{\partial t^2} + k_P[u_S(x,t) - u_R(x,t)] = -F_S(x,t), \quad (2)$$

where m_S is the mass of the sleeper per unit length, F_S is the load between the sleepers and the ballast.

The ballast is first considered as Cosserat model by Suiker et al. (1999). The system is written at the top and bottom of the ballast as:

$$\frac{m_B}{6}\left[2\frac{\partial^2 u_S(x,t)}{\partial t^2} + \frac{\partial^2 u_B(x,t)}{\partial t^2}\right] + k_B[u_S(x,t) - u_R(x,t)] = F_S(x,t), \quad (3)$$

$$\frac{m_B}{6}\left[\frac{\partial^2 u_S(x,t)}{\partial t^2} + 2\frac{\partial^2 u_B(x,t)}{\partial t^2}\right] + k_B[-u_S(x,t) + u_B(x,t)] = -F_B(x,t), \quad (4)$$

in which m_B is the mass of the ballast per unit length, k_B is the spring constant between ballast and sleepers, F_B is the ballast load on the soil, and u_B is the vertical displacement of the ballast.

Based on the assumption of neglecting the apparent mass density, the linearized dynamic equations of motion for a fully saturated poroelastic soil medium are given by Biot (1956) as:

$$\mu u_{i,jj} + (\lambda + \alpha^2 M + \mu) u_{j,ji} + \alpha M w_{j,ji} = \rho \ddot{u}_i + \rho_f \ddot{w}_i, \tag{5}$$

$$\alpha M u_{j,ji} + M w_{j,ji} = \rho_f \ddot{u}_i + m \ddot{w}_i + b \dot{w}_i, \tag{6}$$

where, u_i, w_i ($i = x, y, z$) are the solid displacement components and fluid displacement relative to solid displacement along the x, y, and z directions; dots on u_i and w_i indicate the differential with respect to time t; λ and μ are Lame constants; α and M are Biot's parameters accounting for compressibility of the two-phased material; $\rho = n\rho_f + (1-n)\rho_s$, where ρ_f and ρ_s are the mass densities of the fluid and solid and n is the porosity; m is a density-like parameter that depends on $\rho_f$and the geometry of the pores; b is a parameter accounting for the internal friction due to the relative motion between the solid and the pore fluid. The parameter b equals to the ratio between the fluid viscosity and the intrinsic permeability of the medium ($b = 0$ for the neglect of internal friction). The constitutive relations can be expressed as:

$$\sigma_{ij} = \lambda \delta_{ij} \theta + \mu(u_{i,j} + u_{j,i}) - \alpha \delta_{ij} p, \tag{7}$$

$$p = -\alpha M \theta + M \varsigma, \tag{8}$$

$$\varsigma = -w_{i,i}, \tag{9}$$

where $\theta = u_{i,\,i}$ is solid strain; σ_{ij} is the total stress component of bulk material; p is the pore water pressure.

In this article, the dimensionless variations are adopted. All the displacements are non-dimensionalized with respect to the unit length a. Pore water pressures and stresses are non-dimensionalized with respect to the shear modulus μ. The load between the rail, sleeper, ballast, and ground are non-dimensionalized with respect to μa^2. All variables are then replaced by appropriate dimensionless quantities, denoted by the superscript asterisk (*). The dimensionless time is defined as:

$$\tau = (t/a)\sqrt{\mu/\rho}. \tag{10}$$

The following non-dimensional parameters are also introduced: $k_B^* = \frac{k_B}{\mu a}$, $k_P^* = \frac{k_P}{\mu a}$, $\lambda^* = \frac{\lambda}{\mu}$, $M^* = \frac{M}{\mu}$, $\rho^* = \frac{\rho_f}{\rho}$, $m^* = \frac{m}{\rho}$, $b^* = \frac{ab}{\sqrt{\rho\mu}}$, $\delta = \frac{EI}{\mu a^2}$, $m_R^* = \frac{m_R^*}{\rho a^2}$, $m_S^* = \frac{m_S^*}{\rho a^2}$, $c_0 = c/V_s$, V_s is the shear wave velocity of the half-space, expressed as $V_s = \sqrt{\mu/\rho_s}$, c is the vehicle speed.

The governing equations of the track and poroelastic half-space are solved by Fourier transform. The details of the process to solve the governing equations are given in Cai et al. (2008). The expression of the rail and the ground surface in the transformed domain is obtained as:

$$\bar{\tilde{u}}_R^*(\xi,\omega) = \frac{-(\alpha_2(\xi,\omega)\alpha_4(\xi,\omega)^2 - \alpha_2(\xi,\omega)\alpha_3(\xi,\omega)\alpha_5(\xi,\omega) - \alpha_4(\xi,\omega)\bar{\bar{F}}_B^*(\xi,\omega)k_p^{*})}{(\alpha_1(\xi,\omega)\alpha_4(\xi,\omega)^2 - \alpha_1(\xi,\omega)\alpha_3(\xi,\omega)\alpha_5(\xi,\omega) + \alpha_5(\xi,\omega)k_p^{*2})}, \tag{11}$$

$$\bar{\bar{\tilde{u}}}_z(\xi,\eta,z^*,\omega) = -\frac{\bar{\Pi}(\eta)}{2a_B}\bar{\bar{F}}_B^*(\xi,\omega)\phi(\xi,\eta,z^*,\omega), \tag{12}$$

where

$$\bar{\bar{F}}_B^*(\xi,\omega) = \frac{\alpha_2(\xi,\omega)\alpha_4(\xi,\omega)k_p^*}{\alpha_1(\xi,\omega)\alpha_6(\xi,\omega)\alpha_4^2(\xi,\omega) - (\alpha_3(\xi,\omega)\alpha_1(\xi,\omega) - k_p^{*2})(1+\alpha_5(\xi,\omega)\alpha_6(\xi,\omega))} \tag{13}$$

ξ, η, ω are variations in the transformed domain corresponding to x^*, y^*, τ in the physical domain. The variations of α_1, α_2, α_3, α_4, α_5, α_6, $\phi(\xi, \eta, z^*, \omega)$ are presented in the Appendix A.

The Fourier spectrum of the rail displacement can be obtained by applying inverse Fourier transform to Eq. (11) with respect to ξ, and the Fourier spectrum of the ground surface displacement can be obtained by applying inverse Fourier transform to Eq. (12) with respect to ξ and η. The Fourier spectrums can be expressed as:

$$\tilde{u}_R^*(x,\omega) = \frac{1}{c_0}\bar{\tilde{u}}_R^*\left(\frac{\Omega-\omega}{c_0},\omega\right)e^{i\left(\frac{\Omega-\omega}{c_0}\right)x}, \tag{14}$$

$$\tilde{u}_z(x,y,0,\omega) = \frac{1}{2\pi c_0}\int_{-\infty}^{\infty} -\frac{\bar{\Pi}(\eta)}{2a_B}\bar{\bar{F}}_B^*\left(\frac{\Omega-\omega}{c_0},\omega\right) \times \phi\left(\frac{\Omega-\omega}{c_0},\eta,0,\omega\right)d\eta \cdot e^{i\left(\frac{\Omega-\omega}{c_0}\right)x}. \tag{15}$$

The displacement of the rail and ground in the time domain can be expressed as follows:

$$u_R^*(x^*,\tau) = \frac{1}{2\pi}\int_{-\infty}^{\infty}\bar{\tilde{u}}_R^*(\xi,\Omega^*,-\xi c_0)e^{i\xi(x^*-c_0\tau)}d\xi \cdot e^{i\Omega^*\tau}, \tag{16}$$

$$u_z^*(x^*,y^*,z^*,\tau) = \frac{1}{4\pi^2}\int_{-\infty}^{\infty}\int_{-\infty}^{\infty}\bar{\bar{\tilde{u}}}_z^*(\xi,\eta,\Omega^*,-\xi c_0)e^{i\eta y^*}e^{i\xi(x^*-c_0\tau)}d\eta d\xi \cdot e^{i\Omega^*\tau}. \tag{17}$$

By introducing an auxiliary spatial coordinate $x_t^* = x^* - c_0\tau$, Eqs. (16) and (17) can also be expressed as:

$$u_R^*(x^*,\tau) = u_R^{\Omega}(x_t^*)\cdot e^{i\Omega^*\tau}, \tag{18}$$

$$u_z^*(x^*,y^*,z^*,\tau) = u_z^{\Omega}(x_t^*,y^*,z^*)\cdot e^{i\Omega^*\tau}. \tag{19}$$

Eqs. (18) and (19) denote that in the auxiliary spatial coordinate, the displacement of the track–ground system are harmonic and have the same frequency as the dynamic load. Thus, the receptance at the jth wheel–rail contact point due to a unit load at the kth wheel–rail contact point on the rail is determined by

$$\Delta_{jk}^R = u_R^{\Omega}(l_{jk}^*), \tag{20}$$

where

$$l_{jk}^* = a_j^* - a_k^* \tag{21}$$

is the dimensionless distance between the two contact points.

The amplitudes of the displacements at the wheel–rail contact points on the rails are given by

$$\mathbf{z}_R'^*(\Omega^*) = \mathbf{\Delta}^{\mathbf{R}}\mathbf{P}'^*(\Omega^*), \tag{22}$$

where $\mathbf{P}'^*(\Omega^*)$ is the dynamic wheel–rail contact force vector and

$$\mathbf{\Delta}^{\mathbf{R}} = \begin{bmatrix} \Delta_{11}^R & \Delta_{12}^R & \cdots & \Delta_{1N}^R \\ \Delta_{21}^R & \Delta_{22}^R & \cdots & \Delta_{2N}^R \\ \vdots & \vdots & \vdots & \vdots \\ \Delta_{N1}^R & \Delta_{N2}^R & \cdots & \Delta_{NN}^R \end{bmatrix} \tag{23}$$

N is the number of wheelsets of the vehicle. The receptance matrix is non-symmetric due to the load motion.

$$\mathbf{z}_R'^*(\Omega^*) = (z_{R1}'^*(\Omega^*), z_{R2}'^*(\Omega^*), z_{R3}'^*(\Omega^*), \ldots, z_{RN}'^*(\Omega^*))^T \tag{24}$$

represents the displacement vector of the rail at the wheel–rail contact points observed in the auxiliary spatial coordinate.

2.2. Receptances of the vehicle at the wheelsets

The vehicle model used in Sheng et al. (2004) is introduced herein. The vehicles are represented as multiple rigid body systems and the vertical dynamics of the vehicles are coupled to the track ground model by introducing a Hertzian contact spring (Jenkins et al., 1974) between each wheelset and the rail. The differential equation of motion for a single vehicle is given by

$$\mathbf{M_V}\ddot{\mathbf{Z}}_V(t) + \mathbf{K_V}\mathbf{Z}_V(t) = -\mathbf{BP}(t), \tag{25}$$

where $\mathbf{M_V}$ and $\mathbf{K_V}$ denote the mass and stiffness matrices of the vehicle, $\mathbf{Z}_V(t)$ denotes the displacement vector, $\mathbf{P}(t)$ denotes the wheel–rail force vector and $\mathbf{B}$ is a matrix of unit and zero elements (see Appendix B).

The dynamic loads are assumed to be caused by a sinusoidal railhead profile. The profile of the corrugated rail is denoted by $z(x) = Ae^{i(2\pi/\lambda_1)x}$, where λ_1 denotes the wavelength and A is the amplitude. The roughness-induced dynamic loads between the wheel–rail are harmonic loads with angular frequency Ω, where $\Omega = 2\pi c/\lambda_1$, c is the vehicle speed. As being expressed in Sheng et al. (2004), $\{P(t)\}$ and $\{Z_V(t)\}$ can be expressed as: $\mathbf{P}(t) = \mathbf{P}'(\Omega)e^{i\Omega t}$, $\mathbf{Z_V}(t) = \mathbf{Z}'_{\mathbf{V}}(\Omega)e^{i\Omega t}$. Eq. (25) yields

$$\mathbf{Z}'_{\mathbf{V}}(\Omega) = -(\mathbf{K_V} - \Omega^2\mathbf{M_V})^{-1}\mathbf{B}\mathbf{P}'(\Omega). \tag{26}$$

The receptance between the jth and kth wheelsets within a vehicle is denoted by Δ^{W}_{jk}('W' means wheelset), where, $j, k = 1, 2, \ldots, N$; Δ^{W}_{jk} denotes the displacement amplitude of the jth wheelset due to a unit vertical harmonic load with exciting frequency Ω exerted at the kth wheelset. The displacement vector of wheelsets in the vehicle are expressed as

$$\mathbf{Z}'_{\mathbf{W}}(\Omega) = (Z'_{\mathrm{W1}}(\Omega), Z'_{\mathrm{W2}}(\Omega), Z'_{\mathrm{W3}}(\Omega), \ldots, Z'_{\mathrm{WN}}(\Omega))^{\mathrm{T}} \tag{27}$$

and

$$\mathbf{P}'(\Omega) = (P'_1(\Omega), P'_2(\Omega), P'_3(\Omega), \ldots, P'_N(\Omega))^{\mathrm{T}} \tag{28}$$

is the wheel–rail force vector for a single vehicle.

The displacement vector of the wheelsets is part of that for the corresponding vehicle. Therefore, it may be written as

$$\mathbf{Z}'_{\mathbf{W}}(\Omega) = \mathbf{A}\mathbf{Z}'_{\mathbf{V}}(\Omega), \tag{29}$$

where $\mathbf{A}$ is a constant matrix and $\mathbf{A} = \mathbf{B}^{\mathrm{T}}$ (see the Appendix A). Thus

$$\mathbf{Z}'_{\mathbf{W}}(\Omega) = -\mathbf{\Delta}^{\mathbf{W}}\mathbf{P}'(\Omega) = -\mathbf{A}(\mathbf{K_V} - \Omega^2\mathbf{M_V})^{-1}\mathbf{B}\mathbf{P}'(\Omega), \tag{30}$$

$$\mathbf{\Delta}^{\mathbf{W}} = \begin{bmatrix} \Delta^{\mathrm{W}}_{11} & \cdots & \Delta^{\mathrm{W}}_{1N} \\ \vdots & \cdots & \vdots \\ \Delta^{\mathrm{W}}_{N1} & \cdots & \Delta^{\mathrm{W}}_{NN} \end{bmatrix} = \mathbf{A}(\mathbf{K_V} - \Omega^2\mathbf{M_V})^{-1}\mathbf{B}. \tag{31}$$

Eq. (31) gives the receptance matrix at the wheelsets for a single vehicle.

2.3. Coupling of the vehicles and the track–ground system

The vertical profile of the rail irregularities may be decomposed into a spectrum of discrete harmonic components. In this study, a single harmonic component is selected, thus the rail profile can be

Table 1
Dimensionless parameters for the Mk 3 passenger coach.

Mass of the car body, M^*_C	14.36
Pitch inertia moment of the car body, J^*_C	557.05
Mass of each bogie, M^*_B	1.82
Pitch inertia moment of each bogie, J^*_B	1.32
Secondary vertical stiffness per bogie, k^*_2	0.027
Secondary vertical viscous damping, c^*_2	0.32
Primary vertical stiffness per axle, k^*_{s1}	0.0119
Primary vertical viscous damping per axle, c^*_{s1}	0.0036
Primary damper stiffness per axle, k'^*_{s1}	0.47
Distance between bogie centers	2×8
Bogie wheelbase	2×1.3
Mass of each wheelset, M^*_W	0.92
Wheel diameter	0.914

Table 2
Dimensionless parameters for railway track.

Mass of the beam per unite length of track, m^*_{R}	0.08
Bending stiffness of the rail beam, δ	0.42
Loss factor of the rail	0.01
Rail pad stiffness, k^*_{P}	11.67
Rail pad loss factor	0.15
Mass of the sleeper per unit length of the track, m^*_{S}	0.328
Mass of the ballast per unit length of the track, m^*_{B}	0.84
Ballast stiffness per unit length of the track, k^*_{B}	10.5
Loss factor of the ballast	1.0
Contact width of ballast and ground, $2a_{\mathrm{B}}$	2.7
The Hertz contact stiffness, k^*_{Hl}	90

Table 3
Dimensionless parameters for fully water-saturated poroelastic soil medium.

Lame constant, μ^*	1
Lame constant, λ^*	2
Water density, ρ^*_{f}	0.67
Solid density, ρ^*_{s}	1.22
Parameter of soil structure, m^*	1.68
Coefficient of material damping, D	0.02
Ratio between the fluid viscosity and the intrinsic permeability, b^*	10
The parameter for the compressibility of the soil particle, α	0.97
The parameter for the compressibility of the fluid, M^*	12

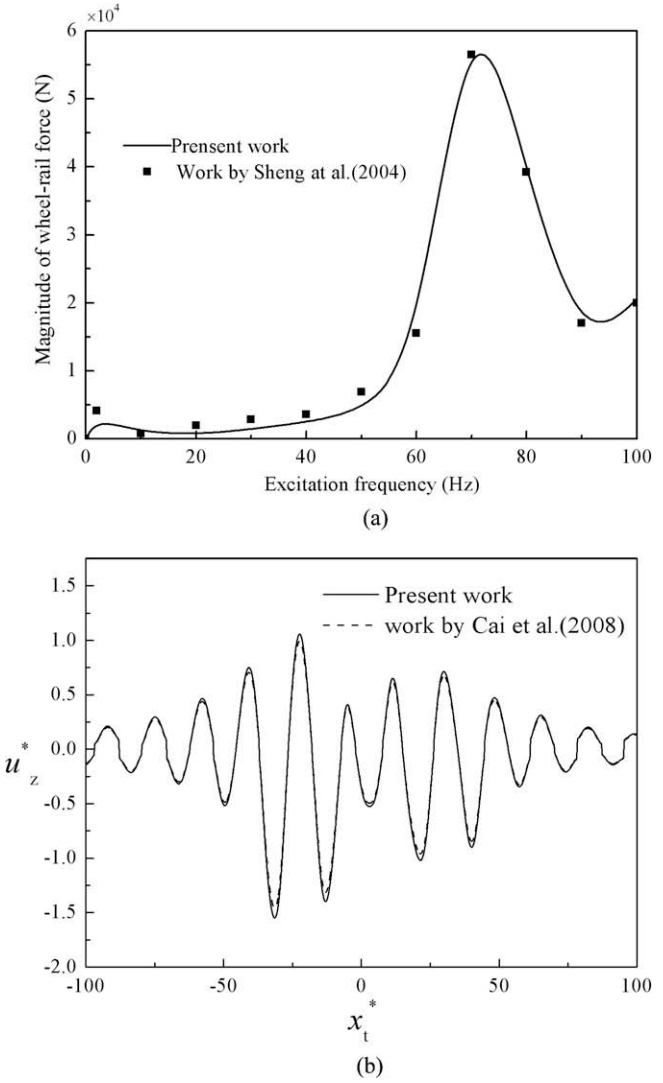

Fig. 2. Comparison with existing work: (a) comparison with Sheng et al. (2004), and (b) comparison with Cai et al. (2008).

express as $z(x) = Ae^{i(2\pi/\lambda_1)x}$. The system is assumed to be linear, so that the displacement input of the sinusoidal rail surface is generated at the excitation frequency $f = c/\lambda_1 = \Omega/2\pi$. At time t, the lth wheelset arrives at $x = a_l + ct$, thus the displacement input at the lth wheel–rail contact point is

$$z_l(t) = z'_l(\Omega)e^{i\Omega t} = Ae^{i(2\pi/\lambda_1)(a_l+ct)} = Ae^{i(2\pi/\lambda_1)a_l}e^{i2\pi(c/\lambda_1)t}. \quad (32)$$

The coupling of a wheelset with rail is illustrated in Fig. 1b, where $z'_{Wl}(\Omega)e^{i\Omega t}$ denotes the displacement of the lth wheelset. The rail and wheel deform locally according to the Hertz theory under the action of the contact force. Thus a Hertzian contact spring is inserted between the wheelset and the rail. Assuming that the dynamic contact force is much smaller compared with the axle load, the Hertz spring can be taken to be linear. The stiffness of the Hertzian contact spring is denoted by k_{Hl}. It is assumed that the wheelset is always in contact with the rail, thus

$$z'_{Wl}(\Omega) = z'_{Rl}(\Omega) + z'_l(\Omega) + P'(\Omega)/k_{Hl}. \quad (33)$$

From Eqs. (22) and (30), the following can be derived

$$z'_{Rl}(\Omega) = \sum_{k=1}^{N} \Delta^{R}_{lk} P'_k(\Omega), \quad (34)$$

$$z'_{Wl}(\Omega) = -\sum_{k=1}^{N} \Delta^{W}_{lk} P'_k(\Omega). \quad (35)$$

By non-dimensionlizing the above equations, the variables are replaced by appropriate dimensionless quantities, denoted by the superscript asterisk (*). And the following non-dimensional parameters are also introduced:

$$\mathbf{K}^*_{\mathbf{V}} = \frac{\mathbf{K}_{\mathbf{V}}}{\mu a}, \quad \mathbf{M}^*_{\mathbf{V}} = \frac{\mathbf{M}_{\mathbf{V}}}{\rho a^3}, \quad k^*_{Hl} = \frac{k_{Hl}}{\mu a}. \quad (36)$$

Substituting Eqs. (34) and (35) into Eq. (33), the following equation can be obtained

$$\sum_{k=1}^{N} (\Delta^{W}_{lk} + \Delta^{R}_{lk}) P^{\prime *}_k(\Omega^*) + P^{\prime *}_l(\Omega^*)/k^*_{Hl} = -z^{\prime *}_l(\Omega^*). \quad (37)$$

The unknowns $Po^{'*}(\Omega^*)$ can be obtained by solving Eq. (37). The displacements of the ground and the rails generated by the dynamic wheel–rail forces are given by applying the superposition principle.

$$u^*_R(x^*, \tau) = \sum_{l=1}^{N} u^{\Omega}_R(x^*_t - a^*_l) P'_l(\Omega^*) e^{i\Omega^*\tau}, \quad (38)$$

$$u^*_z(x^*, \tau) = \sum_{l=1}^{M} u^{\Omega}_z(x^*_t - a^*_l, y^*, z^*) P'_l(\Omega^*) e^{i\Omega^*\tau}. \quad (39)$$

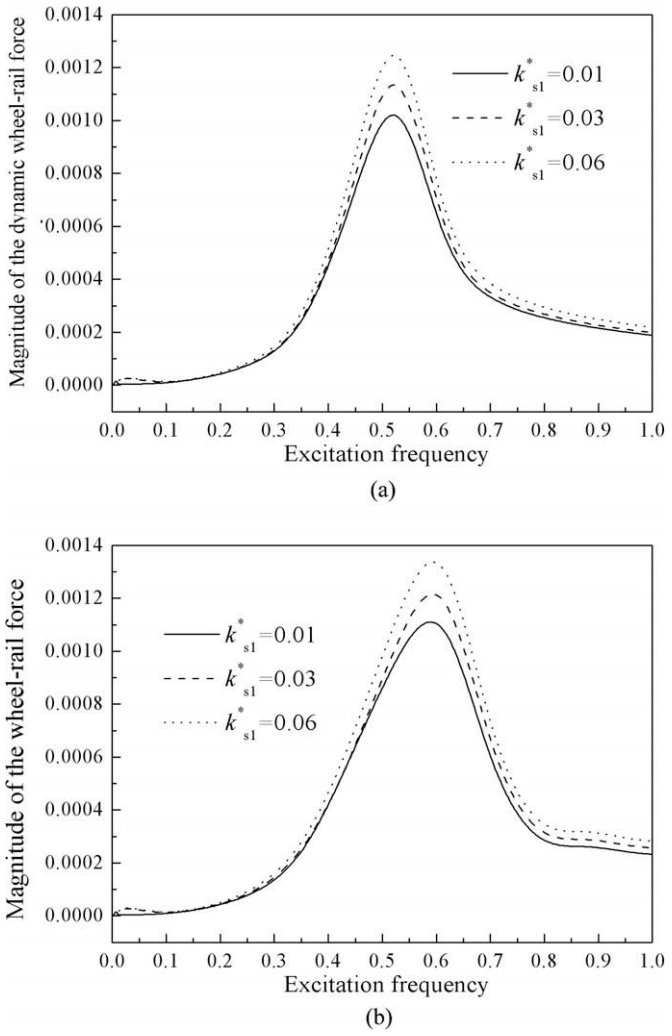

Fig. 3. The effects of the vehicle's primary suspension stiffness k^*_{s1} on the dynamic wheel–rail force.

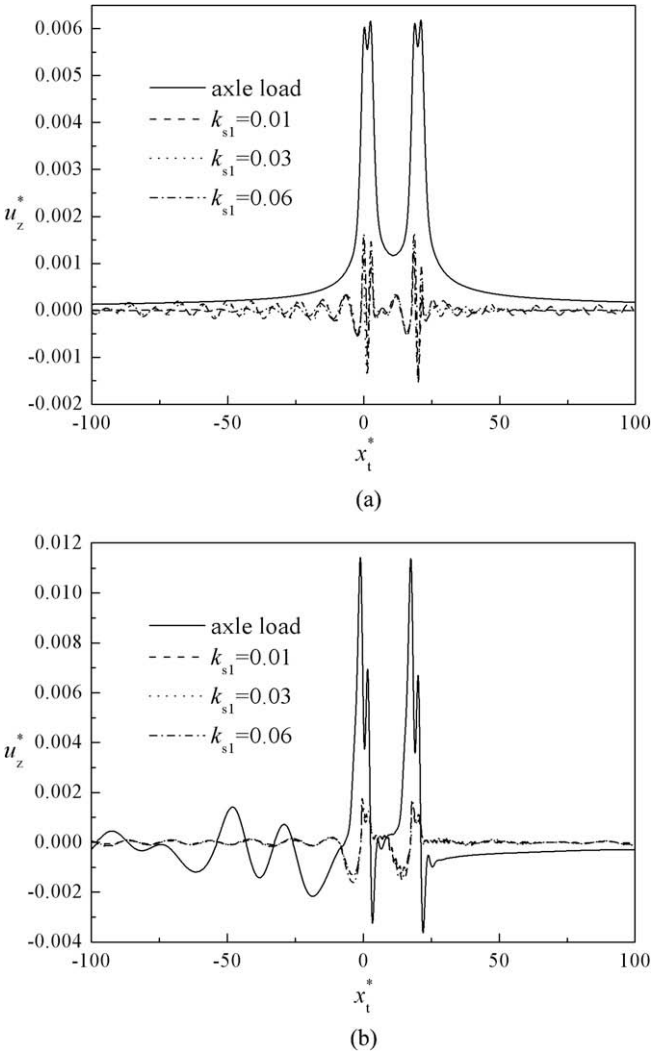

Fig. 4. The effects of the vehicle's primary suspension stiffness on the dynamically induced ground surface displacements: (a) $c_0 = 0.2$ and (b) $c_0 = 1.0$.

3. Results and discussion

For the sake of calculation efficiency and precision, a bogie model is used to calculate the dynamic wheel–rail force in this paper. Assuming that all axles experience the same excitation, apart from a time delay, the dynamic responses of the track system and poroelastic half-space subjected to a single Mk 3 passenger coach are investigated. The parameters for the Mk 3 passenger coach are listed in Table 1 and the parameters for the track are listed in Table 2, corresponding to those used in Sheng et al. (2004). A saturated poroelastic half-space is specified by parameters in Table 3, which are selected refer to Cai et al. (2008). The parameters are selected according to Tables 1–3 if not being denoted in the figures.

3.1. Comparison with existing work

To validate the accuracy of this work, some comparisons with existing work are presented following. In Fig. 2a, the dynamic wheel–rail forces obtained by present model are compared with that given by Sheng et al. (2004). The dynamic wheel–rail force is calculated by single axle vehicle model and the case of an ideal elastic half-space soil medium is simulated by choosing negligibly small values for the poroelastic parameters (ρ_f^*, b^*, M^*, and α are set to 10^{-4}). It can be observed that the two results are in good agreement at the train speed of 60 m/s. In Fig. 2b, the displacements of the poroelastic half-space generated by three X2000 train vehicles are compared with that of Cai et al. (2008) at dimensionless train speed $c_0 = 1.05$. The ground surface displacements are calculated considering the axle load only. The results are normalized with respect to the magnitude of the axle load of locomotive vehicle. Excellent agreement can be observed between the two results.

3.2. The dynamic wheel–rail force

The effects of the primary suspension stiffness of the vehicle on the dynamic wheel–rail forces are investigated in Fig. 3 against the excitation frequency ($f = c/\lambda_1$). In Fig. 3a, the magnitudes of the dynamic wheel–rail force against the excitation frequency for $c_0 = 0.2$ and three kinds of primary suspension stiffness (k_{s1}^*) are presented. It can be seen that the magnitude of the dynamic force increases as the excitation frequency increases and reaches the maximum value at the critical excitation frequency of about 0.55, then decreases rapidly as the excitation frequency increases further. The primary suspension stiffness can affect the dynamic wheel–rail forces

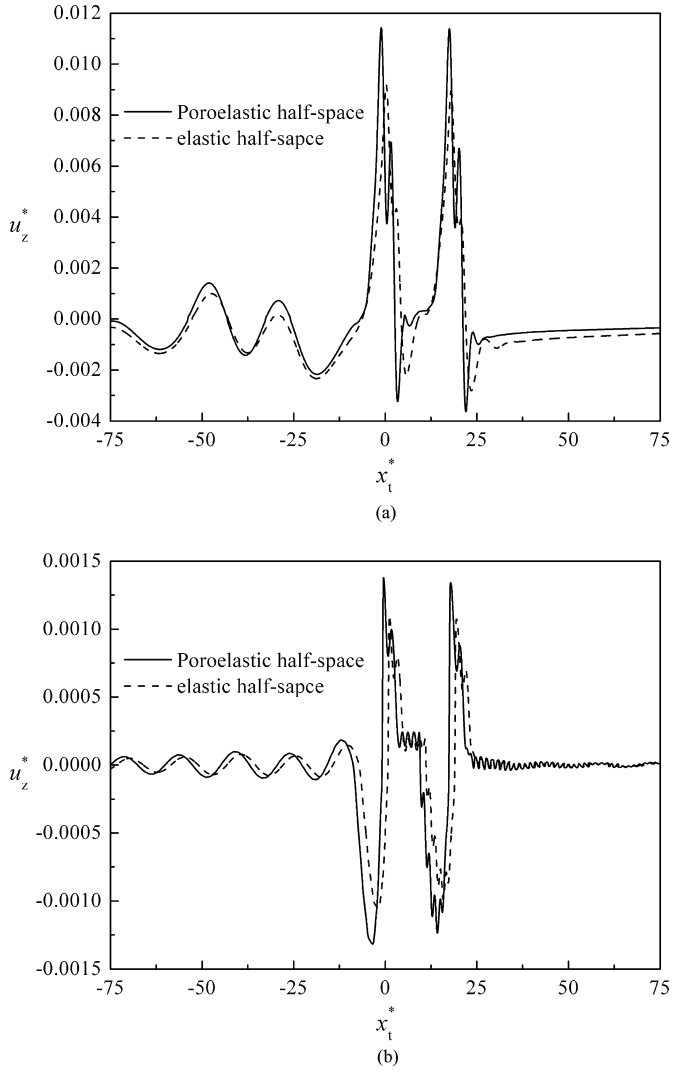

Fig. 5. The comparison between the displacements for poroelastic half-space and elastic half-space: (a) the quasi-statically induced displacement, and (b) the dynamically induced displacement.

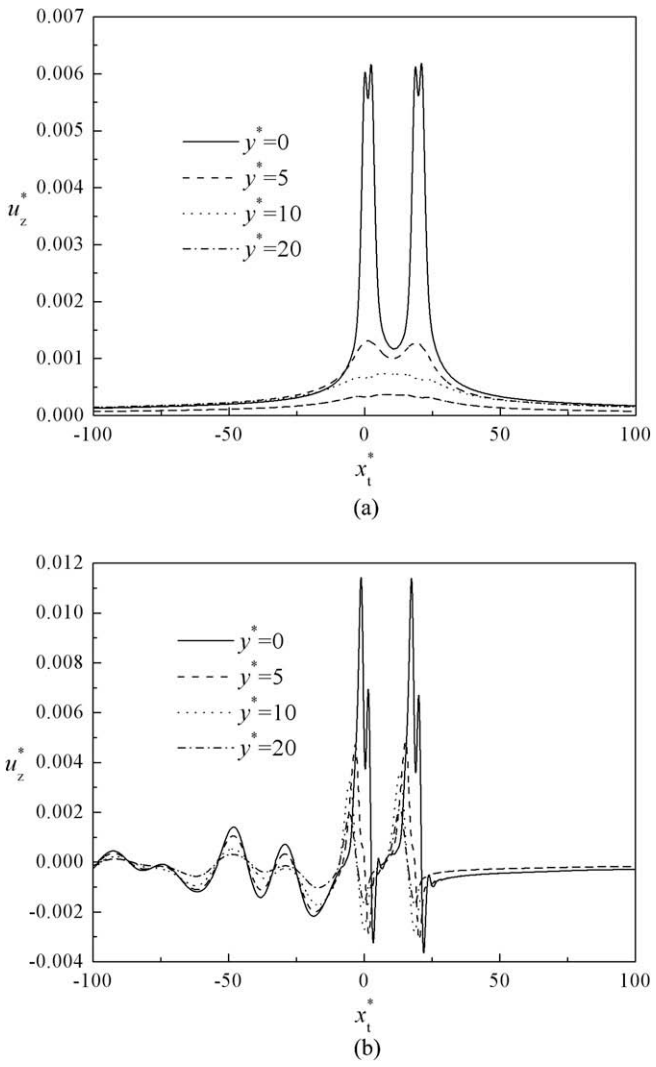

Fig. 6. The quasi-statically induced ground surface displacements for different y^*: (a) $c_0 = 0.2$ and (b) $c_0 = 1.0$.

apparently. The peak value of the dynamic wheel–rail forces increases by 25% as the suspension stiffness increases from 0.01 to 0.006. When the train speed increases to $c_0 = 1.0$, it is shown in Fig. 3b that the magnitude of the dynamic wheel–rail force increases slightly, but the critical excitation frequency increases to 0.6.

3.3. The ground surface displacement response

In order to identify the maximum contribution of the dynamic force to the total response levels, the dynamically induced responses following are all calculated using the maximum dynamic force and its corresponding excitation frequency as input. The total response levels can be obtained by superposition of the dynamically induced components and quasi-statically induced components. In Fig. 4, the effects of the primary suspension stiffness of the vehicle on the dynamically induced ground surface displacement response are investigated, and the quasi-statically induced ground surface displacements are also presented for the sake of comparison. In view of Fig. 4a for $c_0 = 0.2$, a quasi-static deflection appears for the quasi-statically induced displacements and reaches a peak value at the wheel–rail contact point. The dynamically induced displacement fluctuates apparently along the x_t^* axis. The suspension stiffness has considerable effect on the magnitude of the dynamically induced displacement. The maximum value of the dynamically induced displacement increases by about 25% as the suspension stiffness k_{s1}^* increases from 0.01 to 0.06. However, compared with the quasi-statically induced displacement, the dynamically induced displacement is much smaller, about 20% of the quasi-statically induced one. When $c_0 = 1.0$, as shown in Fig. 4b, the quasi-statically induced displacement become much larger and is the dominant components for the displacement responses. The dynamically induced displacement is about 10% of the quasi-statically induced one, and increases as k_{s1}^* increases.

In Fig. 5, the displacements of the ground surface predicted by poroelastic soil model and elastic soil model are compared to show their different characteristics. The results are presented at the train speed $c_0 = 1.0$. It can be seen in Fig. 5 that both the quasi-statically induced and dynamically induced displacement responses for the poroelastic half-space are larger than those for the elastic half-space. This phenomenon is due to the dispersion of Rayleigh-wave of the poroelastic half-space (Jin, 2004). Thus, using the elastic soil model will underestimate both the quasi-statically induced and dynamically induced ground response level.

In order to investigate the different dissipation properties of the quasi-statically and dynamically induced components, the ground surface displacements are presented for various y^* in Figs. 6 and 7,

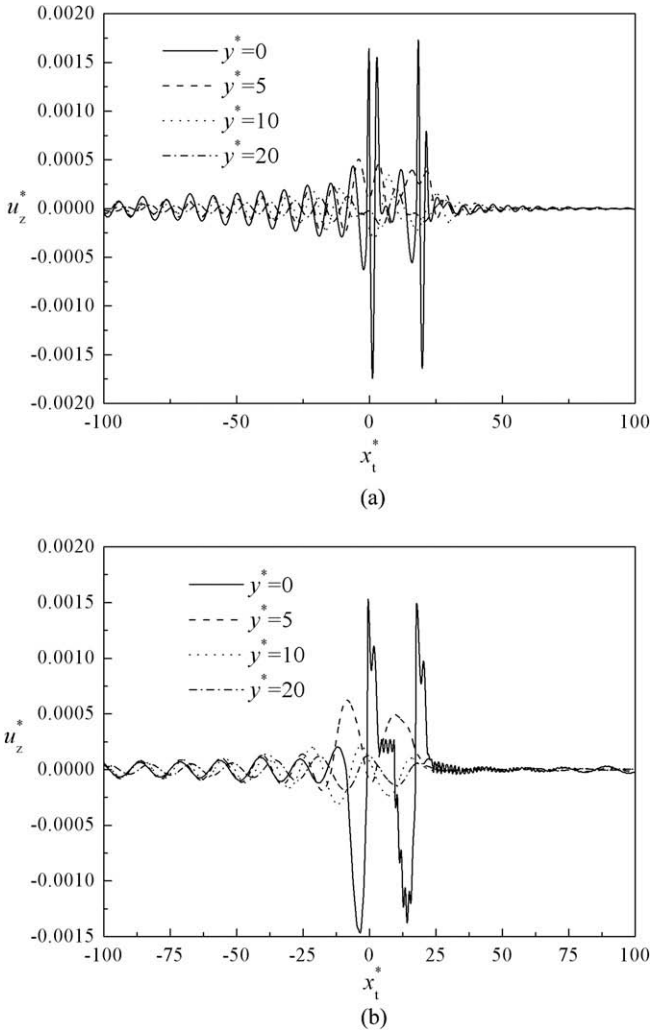

Fig. 7. The dynamically induced ground surface displacements for different y^*: (a) $c_0 = 0.2$ and (b) $c_0 = 1.0$.

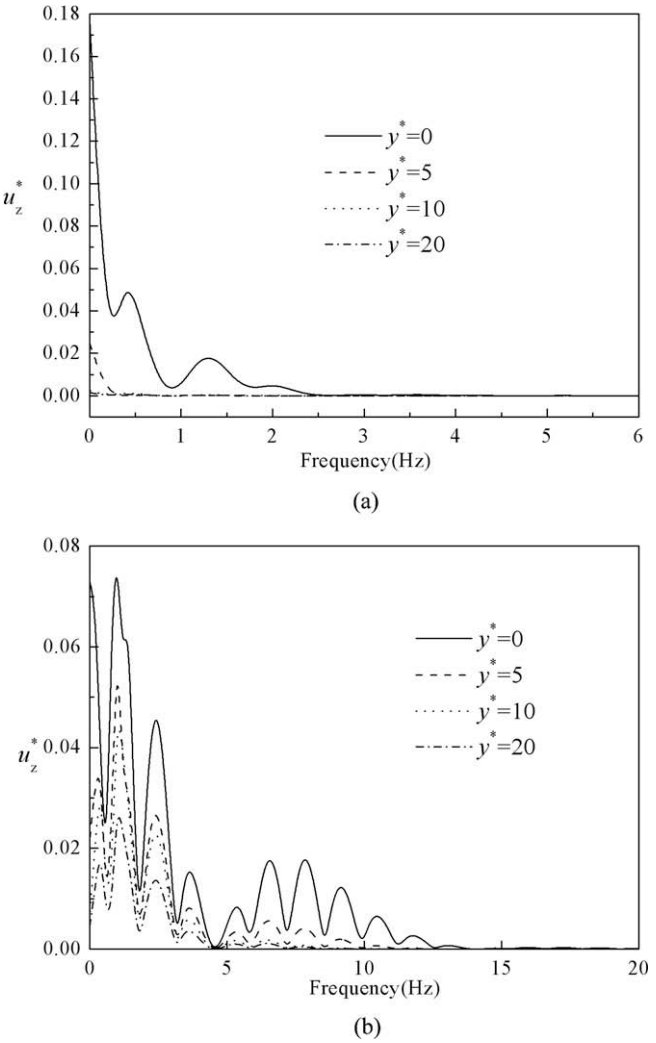

Fig. 8. Fourier amplitudes of quasi-statically induced ground surface displacement for different y^*: (a) $c_0 = 0.2$ and (b) $c_0 = 1.0$.

respectively. y^* is the distance from the track center. In Fig. 6 for the quasi-statically induced displacement, the associated quasi-static deformation appears on the free-field off the track at $c_0 = 0.2$, but deceases in an exponential decay within a short distance. For instance, at the position of $y^* = 10$, only a small deflection remains. However, as the train speed exceeds the critical speed at $c_0 = 1.0$, the free-field response is rather conspicuous with less damping and substantially large at $y^* = 20$. This phenomenon is due to the fact that the body wave and Rayleigh wave are strongly excited by the axle load when the train speed exceeds the critical speed of the track–ground system. The Rayleigh wave is the dominant contribution to the response in a region near the ground surface, which dissipates slowly in the ground. In Fig. 7, the dynamically induced displacements are presented for different y^*. When $c_0 = 0.2$, the dynamically induced displacement is about 20% of the quasi-statically induced displacement at $y^* = 0$ while 50% at $y^* = 20$. Thus, the dynamically induced displacement dissipates more slowly at $c_0 = 0.2$. As the train speed increases to $c_0 = 1.0$, the dynamically induced displacements are much smaller than the quasi-statically induced displacements for various y^*. But it should be noted that the dynamically induced displacements also dissipate slowly at this train speed. This is because that the energies generated by the dynamic load transmit away in the ground mainly through the Rayleigh-wave for both train speed below and above the critical speed.

The Fourier spectrum are also computed and shown for the quasi-statically induced displacement and the dynamically induced displacement in Figs. 8 and 9, respectively. In Fig. 8, the Fourier spectrums of quasi-statically induced ground surface displacement are presented. It is observed that quasi-static response distributes in the frequency range below 2.5 Hz at the train speed $c_0 = 0.2$. The peaks of the spectrum in the figure are associated with the train weight, the train geometry and the distances of bogie position in the vehicles, which are explained specifically in Takemiya and Bian (2005). The amplitude of the Fourier spectrum decreases rapidly as y^* increases and the frequency content of the quasi-statically induced displacement shows a strong shift to lower frequencies with increasing y^*. As the train speed increases to $c_0 = 1.0$, the frequency component shifts proportionally to the train speed, and distribute in the frequency range about 0–15 Hz. The Fourier spectrum of the displacement decreases with distance more slowly for $c_0 = 1.0$. The vibration transmission in the y^* direction is apparent.

In Fig. 9, the Fourier amplitudes of dynamically induced ground surface displacements are presented. From Fig. 9a, when $c_0 = 0.2$, it can be seen that the frequency components of the

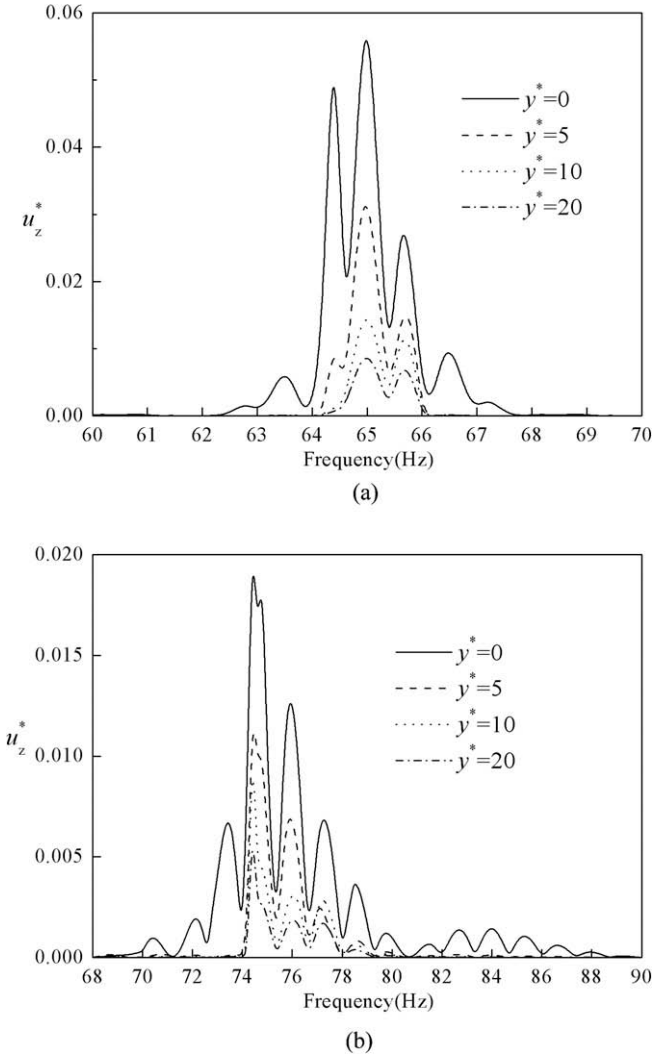

Fig. 9. Fourier amplitudes of dynamically induced ground surface displacement for different y^*: (a) $c_0 = 0.2$ and (b) $c_0 = 1.0$.

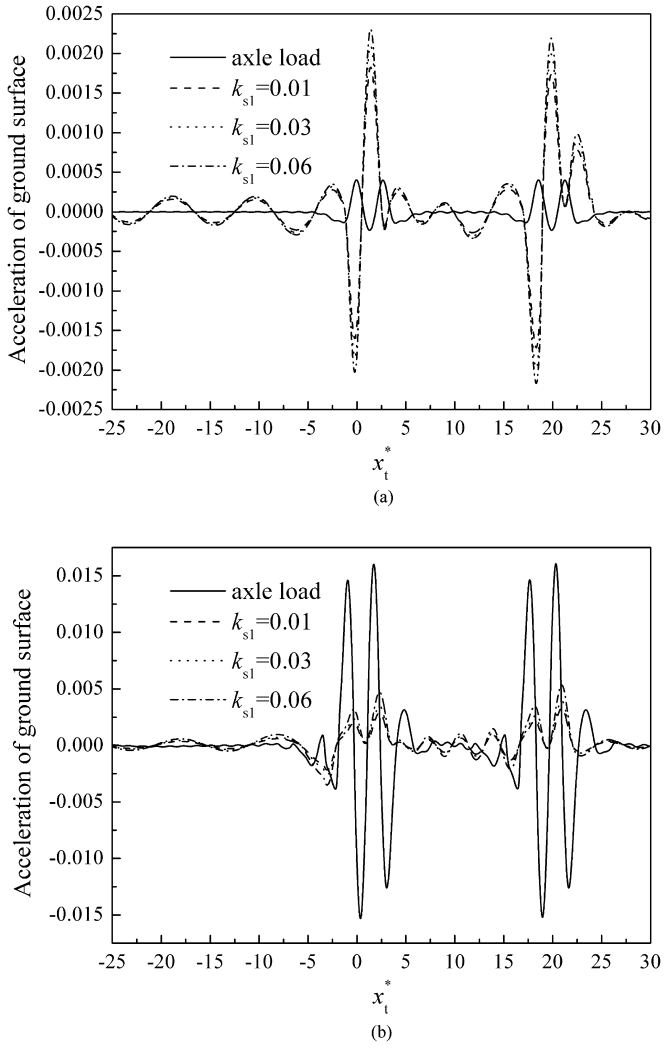

Fig. 10. The effects of the vehicle's primary suspension stiffness on the dynamically induced ground surface accelerations: (a) $c_0 = 0.2$ and (b) $c_0 = 1.0$.

dynamically induced displacement concentrate around the frequency 65 Hz, which is the excitation frequency of the maximum dynamic load at the train speed $c_0 = 0.2$. The Fourier amplitude of the dynamically induced displacement is smaller than that of the quasi-statically induced displacement, but lies in a broader frequency range of about 63–68 Hz. As the train speed increases to $c_0 = 1.0$, the predominant frequency components of the dynamically induced displacement concentrate around 75 Hz, corresponding to the excitation frequency of the maximum dynamic load at $c_0 = 1.0$, and distributes in the range of 70–80 Hz. Thus, the dynamically induced displacement distributes in a much higher frequency range compared with that of quasi-statically induced displacement. It can also be obtained that the Fourier amplitude of the dynamically induced displacement decreases as the train speed increases from $c_0 = 0.2$ to $c_0 = 1.0$. The significant vibration transmissions in y^* direction are clearly visible in Fig. 8 for both $c_0 = 0.2$ and $c_0 = 1.0$.

3.4. The ground surface acceleration response

For environmental protection of the area on the line-side, the train induced ground acceleration response is investigated. In Fig. 10, the effects of the primary suspension stiffness k^*_{s1} on the dynamically induced ground surface accelerations are presented, and the quasi-statically induced accelerations are also shown for comparison. When $c_0 = 0.2$, The dynamically induced accelerations fluctuate apparently within the load area. The suspension stiffness has an apparent effect on the magnitude of dynamically induced accelerations. The magnitude of the dynamically induced accelerations can increases by 30% as k^*_{s1} increases from 0.01 to 0.06. Compared with the quasi-statically induced accelerations, the dynamically induced accelerations are much larger and are the dominant components for the ground vibration. The total acceleration responses decrease apparently as the suspension stiffness decreases. Thus, in view of the train-induced ground vibration, it is of great significance to reduce the primary suspension stiffness if possible. When $c_0 = 1.0$, as shown in Fig. 10b, large ground vibrations are generated by the axle load. The quasi-statically induced accelerations become enormously large and fluctuate conspicuously. They are the dominant components for the ground vibration at this train speed. However, the dynamically induced accelerations can not be neglected at this train speed. The maximum dynamically induced acceleration is about 25% of the maximum quasi-statically induced acceleration. The effect of the suspension stiffness k^*_{s1} on the dynamically induced acceleration is also apparent at $c_0 = 1.0$.

In Fig. 11, the quasi-statically induced ground surface accelerations are presented at different y^*. The quasi-statically induced

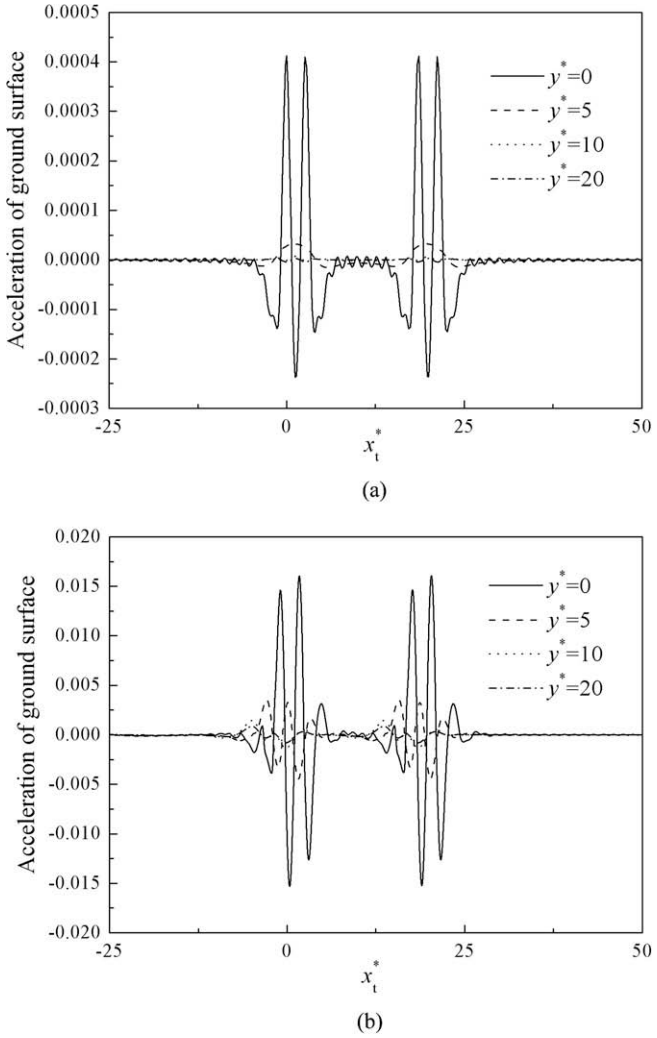

Fig. 11. The quasi-statically induced ground surface accelerations for different y^*: (a) $c_0 = 0.2$ and (b) $c_0 = 1.0$.

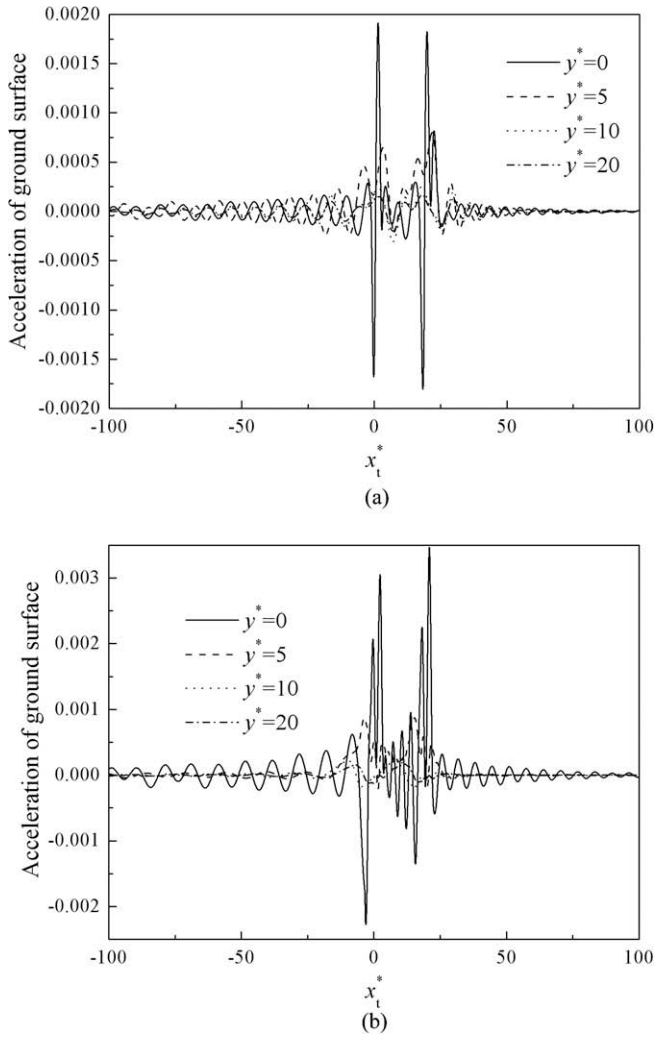

Fig. 12. The dynamically induced ground surface accelerations for different y^*: (a) $c_0 = 0.2$ and (b) $c_0 = 1.0$.

accelerations at $y^* = 0$ gets peak values at the wheel–rail contact point when $c_0 = 0.2$, and the magnitude of the accelerations decays to a very small value within short distance off the track. At train speed $c_0 = 1.0$, the quasi-statically induced accelerations of the ground surface become enormously large and dissipate more slowly in the ground. The ground vibrates apparently even at the place far off the track.

In Fig. 12, the dynamically induced ground surface accelerations are presented at different y^*. For the case of $c_0 = 0.2$, it can be obtained that the acceleration responses fluctuate apparently along the x_t^*. Compared with the quasi-statically induced acceleration, the dynamically induced accelerations are much larger, what is more, the dynamically induced accelerations decay more slowly in the soil. Thus, they become the dominant components for the free-field acceleration responses at the train speed $c_0 = 0.2$. However, as the train speed increases to $c_0 = 1.0$, the dynamically induced accelerations are smaller compared with the quasi-statically induced ones for various y^*. The quasi-statically induced acceleration is the dominant components for the train-induced ground vibration at $c_0 = 1.0$. However, the dynamically induced accelerations can not be neglected, about 20% of the quasi-statically induced accelerations for various y^*. Thus, for low train speed condition, the dynamic load plays a dominant role for the ground surface acceleration response, while as the train speed exceeds the critical speed of the track–ground system, the contribution of dynamic load for the acceleration response is much reduced,, but can not be neglected.

The Fourier spectrum of the quasi-statically and dynamically induced ground surface acceleration is presented in Figs. 13 and 14, respectively. It is noted in Fig. 13 that, for $c_0 = 0.2$, the predominant frequencies of the ground surface acceleration are concentrated at several Hz. However, these frequency components disappear immediately off the track. In the case of $c_0 = 1.0$, the predominant frequencies increase proportionally and distribute in the frequency range of 10–30 Hz, and the above predominant frequencies still dominate the acceleration response as the distance from the track increases. What is more, the Fourier amplitude of the acceleration decreases slowly as y^* increases.

In Fig. 14, the Fourier spectrum of the dynamically induced acceleration is presented. It is seen that the dynamically induced acceleration are dominated by the frequency components of 65–75 Hz at the train speed $c_0 = 0.2$. As the train speed increases to $c_0 = 1.0$, the ground surface acceleration response at $y^* = 0$ distributes in a broad frequency range, while the dynamically induced acceleration off the track are more dominated by frequencies 60–90 Hz than other frequencies. This may be caused from the dynamic track interaction with the Rayleigh wave propagation at

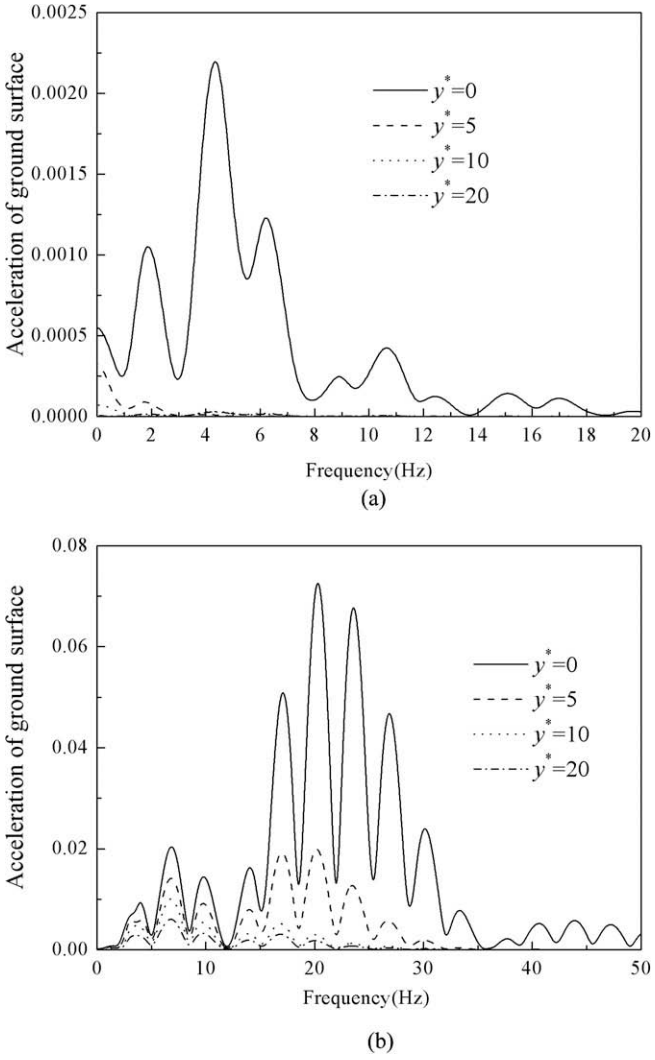

Fig. 13. Fourier amplitudes of quasi-statically induced ground surface accelerations for different y^*: (a) $c_0 = 0.2$ and (b) $c_0 = 1.0$.

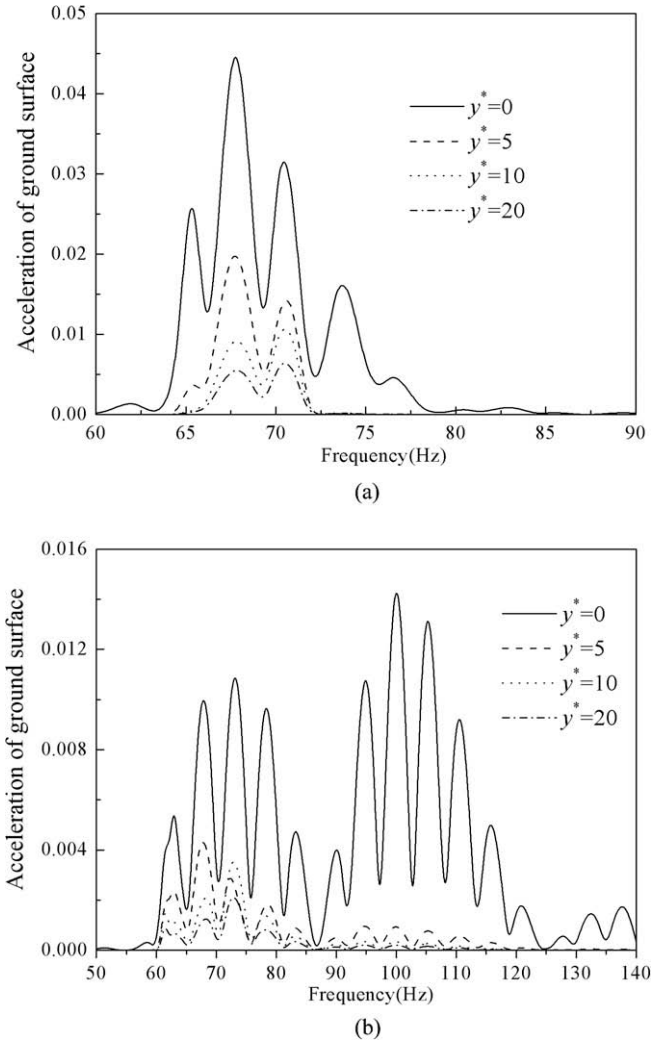

Fig. 14. Fourier amplitudes of dynamically induced ground surface accelerations for different y^*: (a) $c_0 = 0.2$ and (b) $c_0 = 1.0$.

the site. And the Rayleigh wave excited by the dynamic load concentrates at the frequency range about 60–90 Hz.

3.5. The pore water pressure and effective stress response

The different contributions of the axle load and dynamic load to the pore water pressure responses are also investigated in Figs. 15 and 16, and the effects of the soil permeability on the excess pore water pressure responses are also investigated. Fig. 15 shows the vertical variation of the quasi-statically induced excess pore water pressure for three kind of b^*. The maximum pore water pressure occurs at the depth about $z^* = 1$, then diminishes rapidly with depth to a nearly constant value. The pore water pressures increase apparently as b^* increases from 1 to 100. For the depth larger than $z^* = 10$, the pore water pressure responses are small and the effects of b^* on the responses are reduced. It can also be seen that the pore water pressure responses become much lager as the train speed exceeds the critical speed of the track–ground system.

In Fig. 16, the dynamically induced excess pore water pressure is presented. The pore water pressure diminishes rapidly with depth to a constant value after its maximum value has been attained at about $z^* = 1$. It is interesting to note that, at the train speed $c_0 = 0.2$, the peak values of the dynamically induced pore water pressure are larger than that of the quasi-statically induced one for $b^* = 1$ and $b^* = 10$ while smaller for $b^* = 100$. The dynamically induced pore water pressure responses are reduced as the train speed increases from $c_0 = 0.2$ to $c_0 = 1.0$. Compared with the quasi-statically induced pore water pressure, the dynamically induced one at $c_0 = 1.0$ is much smaller. As shown in Fig. 16, It is interesting to note that the effect of the parameter b^* on the dynamically induced pore water pressure is different from that on the quasi-statically induced pore water pressure. The dynamically induced pore water pressure near the ground surface increases rapidly with increasing b^*. However, in the ground deeper than $z^* = 3$, the dynamically induced pore water pressure decreases with increasing b^*. This phenomenon is due to the fact that the energy generated by the dynamic load mainly transmits away by the Rayleigh-wave. Thus, the pore water pressure near the ground surface increasing rapidly as b^* increases (the soil permeability decreases). But as the depth increases, the effect of the surface wave is much reduced. The pore water pressure in the deeper soil is mainly excited by the water flow from the upper soil. It becomes more difficult for the water to flow through the soil skeleton with increasing b^*.

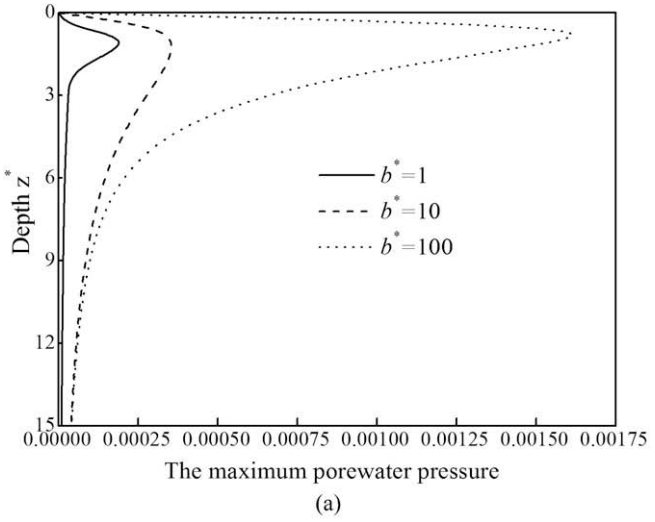

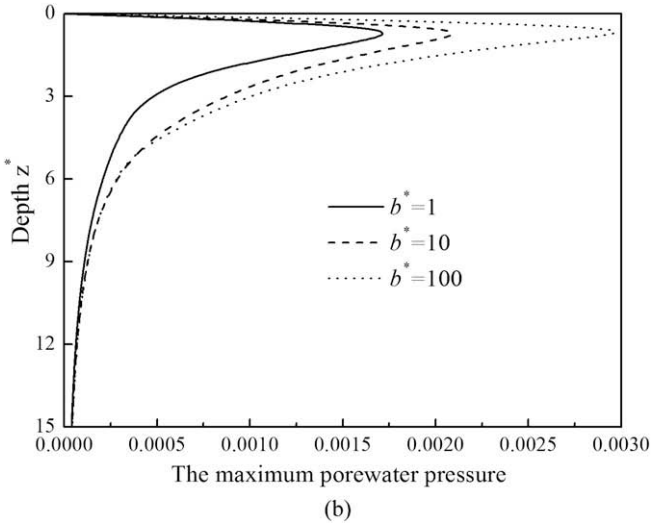

Fig. 15. The quasi-statically induced pore water pressures for different b^*: (a) $c_0 = 0.2$ and (b) $c_0 = 1.0$.

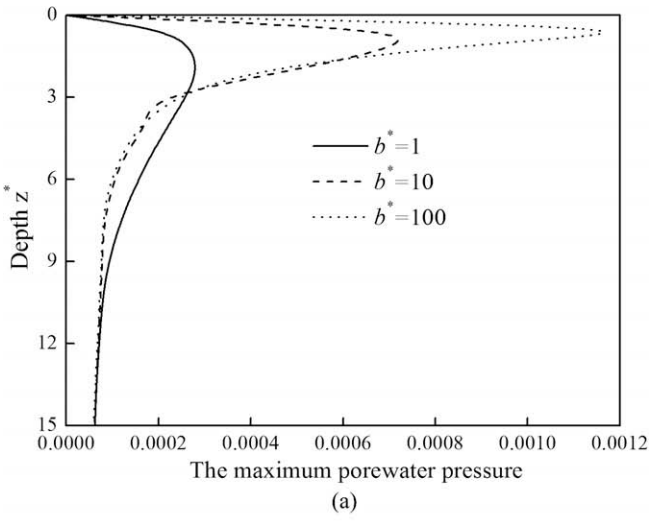

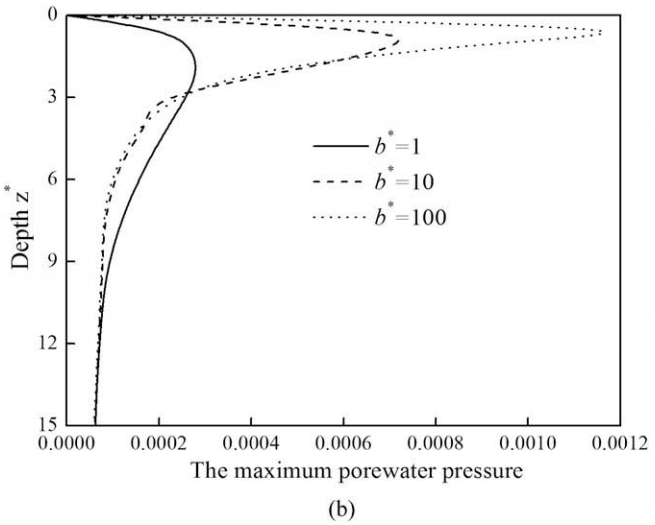

Fig. 16. The dynamically induced pore water pressures for different b^*: (a) $c_0 = 0.2$ and (b) $c_0 = 1.0$.

The quasi-statically induced and dynamically induced effective stresses are presented in Figs. 17 and 18, respectively. In Fig. 17 for the quasi-statically induced stress, the effective stress gets the maximum value at the ground surface and decreases rapidly with increasing depth z^* at $c_0 = 0.2$. The effect of b^* on the effective stress is not obvious. As the train speed increases to $c_0 = 1.0$, the effective stresses become much larger and decrease rapidly as b^* increases from 1 to 100 in the region near the ground surface. As the depth increases, the effective stresses are smaller and the effect of b^* on the effective stress is not obvious. For the dynamically induced effective stress, it can be seen in Fig. 18 that the values of the dynamically induced effective stress at the ground surface are about 40% of the quasi-statically induced effective stress at $c_0 = 0.2$, as the train speed increases to $c_0 = 1.0$, the percent of the dynamically induced effective stress is reduced, about 25%. The dynamically induced effective stresses decrease to smaller value at the depth $z^* = 10$. Thus, the dynamic load plays an important role for the train-induced effective stress in the subsoil and should not be neglected when predicting the train-induced effective stress.

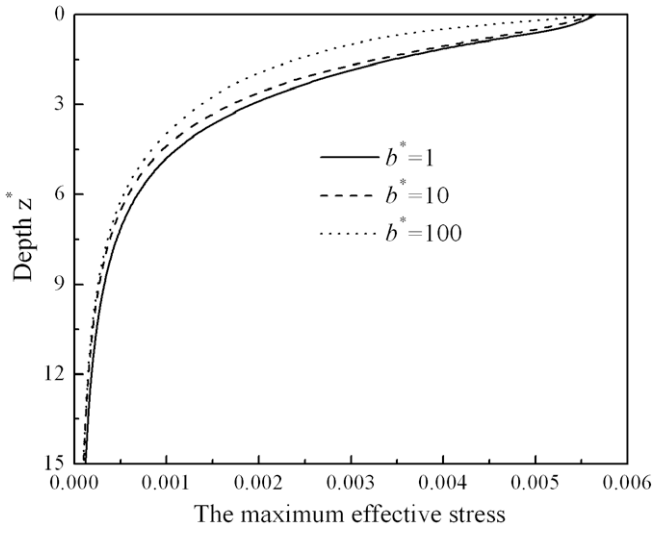

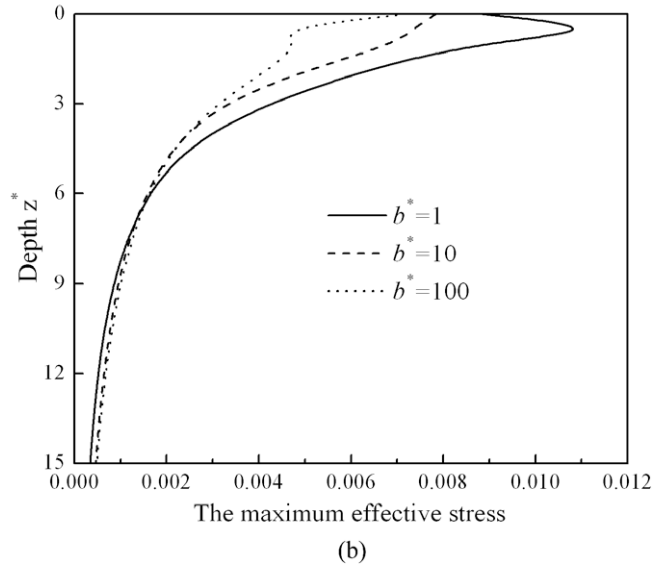

Fig. 17. The quasi-statically induced effective stress for different b^*: (a) $c_0 = 0.2$ and (b) $c_0 = 1.0$.

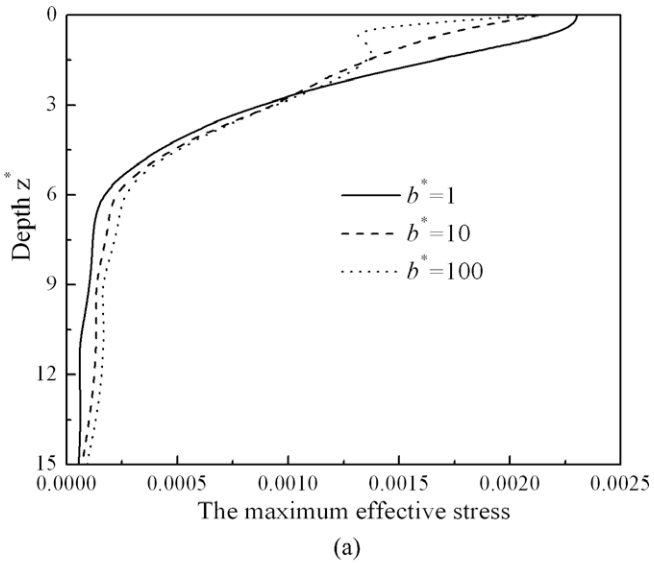

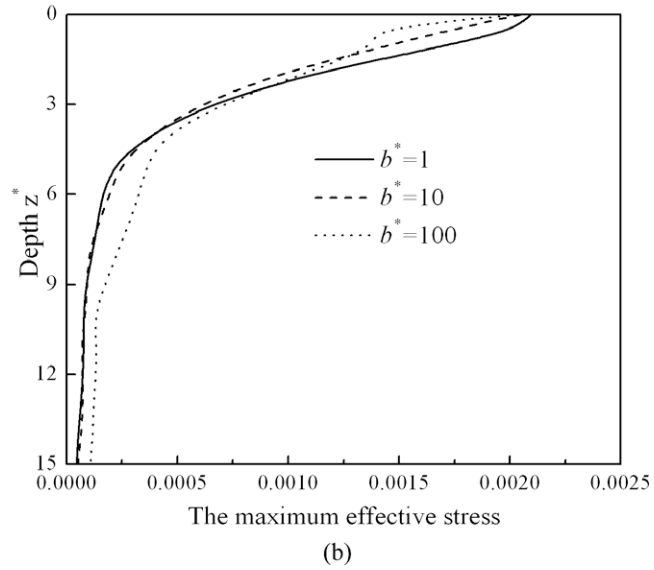

Fig. 18. The dynamically induced effective stress for different b^*: (a) $c_0 = 0.2$ and (b) $c_0 = 1.0$.

4. Conclusions

In this paper, dynamic responses of the poroelastic half-space soil medium subjected to the quasi-static and dynamic loads from moving train are investigated using a vehicle–track–ground coupling model. The governing equations are solved by Fourier transform and the time-domain results are calculated by fast inverse Fourier transform. The different roles of the axle loads and dynamic loads for the ground vibration are identified at the vehicle speed below and above critical speed. The effects of primary suspension stiffness and the soil permeability on the dynamic responses are investigated systematically. The frequency contents of the quasi-statically and dynamically induced response are also studied. The main conclusions of this study can be summarized as follows:

1. For the train speed below the critical speed, the axle loads are the dominant excitations for the ground displacement responses. While the dynamic loads are the dominant excitations for the ground surface acceleration responses, especially

at free field off the track as the dynamically induced accelerations dissipate more slowly in the ground. However, as the train speed exceeds the critical speed, the contributions of the dynamic loads to the ground displacement and acceleration responses are much smaller than that of quasi-static loads.

2. The increase of the primary suspension stiffness can intensify the dynamic interaction between the wheel and rail. Furthermore, the ground surface accelerations increase apparently as the primary suspension stiffness increases. For the train speed below the critical speed, reducing the primary suspension stiffness can lessen the train-induced ground vibration efficiently.
3. The quasi-statically induced displacement lies in the low frequency range about 0–15 Hz. But the dynamically induced displacement distributes in a much higher frequency range of above 60 Hz, which depends on the train speed. The predominant frequencies of the quasi-statically induced acceleration concentrate at several Hz for the train speed $c_0 = 0.2$ and 15–35 Hz for $c_0 = 1.0$, while the predominant frequencies of dynamically induced acceleration distributes in the frequency range of 65–75 Hz at $c_0 = 0.2$ and 60–90 Hz at $c_0 = 1.0$.
4. The dynamic loads make significant contribution to the pore water pressure and effective stress response in the subsoil at both the train speed below and above the critical speed, and cannot be neglected for the prediction of the train-induced effective stress in the subsoil.

Acknowledgments

The work presented in this paper is supported by the National Natural Science Foundation of China (Grant No. 50778136) and the Nature Science Foundation of Zhejiang Province (Grant No. R1080819).

Appendix A

$$\left.\begin{aligned}
&\alpha_1(\xi,\omega) = \delta\xi^4 - m_{\mathrm{R}}^*\omega^2 + k_{\mathrm{P}}^*\\
&\alpha_2(\xi,\omega) = 2\pi\delta(\omega + \varepsilon c_0 - \Omega)\\
&\alpha_3(\xi,\omega) = -m_{\mathrm{B}}^*\omega^2/2 + k_{\mathrm{P}}^* + k_{\mathrm{B}}^* - m_{\mathrm{S}}^*\omega^2\\
&\alpha_4(\xi,\omega) = -m_{\mathrm{B}}^*\omega^2/6 - k_{\mathrm{B}}^*\\
&\alpha_5(\xi,\omega) = -m_{\mathrm{B}}^*\omega^2/3 + k_{\mathrm{B}}^*\\
&\alpha_6(\xi,\omega) = \Psi(\xi,0,\omega)
\end{aligned}\right\}, \tag{A.1}$$

$$\Psi(\xi,0,\omega) = \frac{1}{2\pi}\int_{-\infty}^{\infty} -\overline{\Pi}^2(\eta)\phi(\xi,\eta,0,\omega)\mathrm{e}^{\mathrm{i}\eta y^*}\,\mathrm{d}y, \tag{A.2}$$

$$\begin{aligned}
\phi(\xi,\eta,z^*,\omega) = \frac{1}{\Delta}[&(\gamma_3^2 + \xi^2 + \eta^2)(\gamma_2 a_2 \mathrm{e}^{-\gamma_2 z^*} - \gamma_1 a_1 \mathrm{e}^{-\gamma_1 z^*})\\
&+ (\gamma_1 g_5 - \gamma_2 g_6)\mathrm{e}^{-\gamma_3 z^*}],
\end{aligned} \tag{A.3}$$

$$\gamma_i = \sqrt{\xi^2 + \eta^2 - b_i^2}\ i = 1,2, \tag{A.4}$$

$$\gamma_3 = \sqrt{\xi^2 + \eta^2 + D^2}, \tag{A.5}$$

$$\left.\begin{aligned}
a_1 &= \frac{(m^*\omega^2 - \mathrm{i}b^*\omega)(\lambda^* + \alpha^2 M^* + 2) + M^*\omega^2 - 2\alpha M^*\rho^*\omega^2}{(\lambda^* + 2)M^*}\\
a_2 &= \frac{(m^*\omega^2 - \mathrm{i}b^*\omega)\omega^2 - (\rho^*)^2\omega^4}{(\lambda^* + 2)M^*}
\end{aligned}\right\}, \tag{A.6}$$

$$\Delta = (g_4 - g_3)(\gamma_3^2 + \xi^2 + \eta^2) - 2\gamma_3(\gamma_1 g_5 - \gamma_2 g_6), \tag{A.7}$$

$$g_i = E_i + (2\xi^2 - b_i^2)F_i\ i = 1,2, \tag{A.8}$$

$$\left.\begin{aligned}
g_3 &= \lambda^* E_1 - 2\gamma_1^2 F_1 - \alpha\\
g_4 &= \lambda^* E_2 - 2\gamma_2^2 F_2 - \alpha\\
g_5 &= g_1 + 2\eta^2 a_1\\
g_6 &= g_2 + 2\eta^2 a_2
\end{aligned}\right\}, \tag{A.9}$$

$$E_i = \frac{\vartheta M^* b_i^2 - \rho^*\omega^2}{\rho^*\Omega^2(\alpha - \vartheta)M^*}\ i = 1,2, \tag{A.10}$$

$$F_i = \frac{\lambda^* E_i + E_i - \alpha + \vartheta}{D^2 - b_i^2}\ i = 1,2, \tag{A.11}$$

$$b_1^2 = \frac{a_1 + \sqrt{a_1^2 - 4a_2}}{2}, \quad b_2^2 = \frac{a_1 - \sqrt{a_1^2 - 4a_2}}{2}, \tag{A.12}$$

$$D^2 = (1 - \rho^*\vartheta)\omega^2, \tag{A.13}$$

$$\vartheta = \rho^*\omega^2/(m^*\omega^2 - \mathrm{i}b^*\omega). \tag{A.14}$$

The explanations of these expressions can be found in detail in Cai et al. (2008).

Appendix B

The details and parameters of the vehicle are shown in Fig. 19. The displacement vector of the vehicle is defined as

$$\begin{aligned}
\mathbf{Z_V}(t) = (&Z_{\mathrm{C}}(t), \varphi_{\mathrm{C}}(t), Z_{\mathrm{B1}}(t), \varphi_{\mathrm{B1}}(t), Z_{\mathrm{B2}}(t), \varphi_{\mathrm{B2}}(t), Z_{\mathrm{W1}}(t), Z_{\mathrm{W2}}(t),\\
&Z_{\mathrm{W3}}(t), Z_{\mathrm{W4}}(t)).
\end{aligned} \tag{B.1}$$

Corresponding to this displacement vector, the external load vector is determined as

$$\begin{aligned}
\mathbf{F_V}(t) &= (0,0,0,0,0,0,-P_1(t),-P_2(t),-P_3(t),-P_4(t))^{\mathrm{T}}\\
&= -\mathbf{B}\mathbf{P}(t).
\end{aligned} \tag{B.2}$$

where

$$\mathbf{B} = \begin{bmatrix}\mathbf{0}_{6\times4}\\ \mathbf{I}_{4\times4}\end{bmatrix} \tag{B.3}$$

and

$$\mathbf{P}(t) = (P_1(t), P_2(t), P_3(t), P_4(t))^{\mathrm{T}} \tag{B.4}$$

is the vertical wheel–rail load vector.

The wheelset displacement vector can be written as

$$\mathbf{Z_W}(t) = \mathbf{A}\mathbf{Z_V}(t), \tag{B.5}$$

where

$$\mathbf{A} = [\mathbf{0}_{4\times6}\ \mathbf{I}_{4\times4}] = \mathbf{B}^{\mathrm{T}}. \tag{B.6}$$

The mass matrix is given by

$$\mathbf{M_V} = \mathrm{diag}(M_{\mathrm{C}}, J_{\mathrm{C}}, M_{\mathrm{B}}, J_{\mathrm{B}}, M_{\mathrm{B}}, J_{\mathrm{B}}, M_{\mathrm{W}}, M_{\mathrm{W}}, M_{\mathrm{W}}, M_{\mathrm{W}}). \tag{B.7}$$

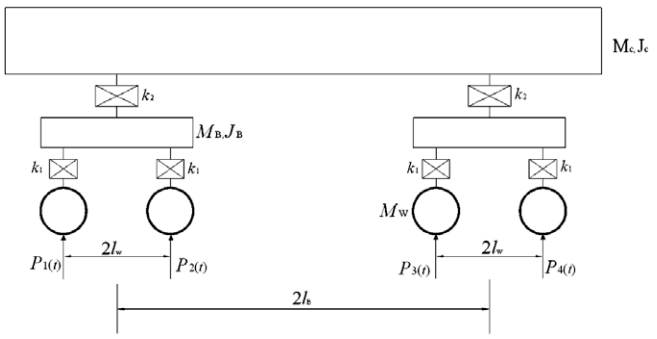

Fig. 19. The details of the vehicle dynamics model.

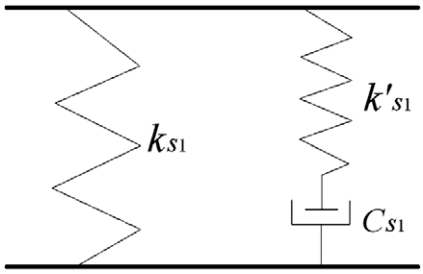

Fig. 20. The structure of primary suspension.

The stiffness matrix is given by

$$[K_V] = \begin{bmatrix} 2k_2 & 0 & -k_2 & 0 & -k_2 & 0 & 0 & 0 & 0 & 0 \\ 0 & 2k_2 l_B^2 & -k_2 l_B & 0 & k_2 l_B & 0 & 0 & 0 & 0 & 0 \\ -k_2 & -k_2 l_B & k_2+2k_1 & 0 & 0 & 0 & -k_1 & -k_1 & 0 & 0 \\ 0 & 0 & 0 & 2k_1 l_W^2 & 0 & 0 & -k_1 l_w & k_1 l_w & 0 & 0 \\ -k_2 & k_2 l_B & 0 & 0 & k_2+2k_1 & 0 & 0 & 0 & -k_1 & -k_1 \\ 0 & 0 & 0 & 0 & 0 & 2k_1 l_W 2 & 0 & 0 & -k_1 l_w & k_1 l_w \\ 0 & 0 & -k_1 & -k_1 l_w & 0 & 0 & k_1 & 0 & 0 & 0 \\ 0 & 0 & -k_1 & k_1 l_w & 0 & 0 & 0 & k_1 & 0 & 0 \\ 0 & 0 & 0 & 0 & -k_1 & -k_1 l_w & 0 & 0 & k_1 & 0 \\ 0 & 0 & 0 & 0 & -k_1 & k_1 l_w & 0 & 0 & 0 & k_1 \end{bmatrix}. \tag{B.8}$$

The structure of primary suspension is shown in Fig. 20

$$k_1 = \frac{k_{S1}k'_{S1} + i\Omega c_{S1}(k_{S1}+k'_{S1})}{k'_{S1} + i\Omega c_{S1}}. \tag{B.9}$$

The hysteretic damping of second suspension can be incorporated into the suspension by introducing complex spring stiffness.

$$k_2 = k_{S2} + i\Omega c_{S2}. \tag{B.10}$$

References

Biot, M.A., 1956. Theory of propagation of elastic waves in a fluid-saturated porous solid. Part I: Low-frequency range; Part II: High-frequency range. Journal of the Acoustical Society of America 28, 168–191.

Biot, M.A., 1962. Mechanics of deformation and acoustic propagation in porous media. Journal of Applied Physics 33, 1482–1498.

Burke, M., Kingsbury, H.B., 1984. Response of poroelastic layers to moving loads. International Journal of Solids and Structures 20, 499–511.

Cai, Y., Sun, H., Xu, C., 2008. Three dimensional analysis of dynamic responses of track ground system subjected to a moving train load. Computers and Structures 836, 816–824.

Cai, Y., Sun, H., Xu, C., 2009. Three dimensional steady state response of railway system on layered half-space soil medium subjected to a moving train. International Journal for Numerical and Analytical Methods in Geomechanics 33 (4), 529–550.

Chai, J., Miura, N., 2002. Traffic-load-induced permanent deformation of road on soft subsoil. Journal of Geotechnical and Geoenvironmental Engineering 128 (11), 907–916.

Jenkins, H.H., Stephenson, J.E., Clayton, G.A., Morland, G.W., Lyon, D., 1974. The effect of track and vehicle parameters on wheel/rail vertical dynamic loads. Rail Engineering Journal 3 (1), 2–16.

Jin, B., 2004. Dynamic response of a poroelastic half space generated by high speed load. Chinese Quarterly of Mechanics 25, 168–174 (in Chinese).

Kargarnovin, M.H., Younesian, D., 2004. Dynamics of Timoshenko beams on Pasternak foundation under moving load. Mechanics Research Communications 31 (6), 713–723.

Kargarnovin, M.H., Younesian, D., Thompson, D.J., Jones, C.J.C., 2005. Response of beams on nonlinear viscoelastic foundations to harmonic moving loads. Computers and Structures 83 (23–24), 1865–1877.

Katou, M., Matsuoka, T., Yoshioka, O., Sanada, Y., Miyoshi, T., 2008. Numerical simulation study of ground vibrations using forces from wheels of a running high-speed train. Journal of Sound and Vibration 318, 830–849.

Knothe, K., Grassie, S.L., 1993. Modelling of railway track and vehicle track interaction at high frequencies. Vehicle System Dynamics 22, 209–262.

Krylov, V., 1995. Generation of ground vibrations by superfast trains. Applied Acoustics 44, 149–164.

Lombaert, G., Degrand, G., 2009. Ground-brone vibration due to static and dynamic axle loads of InterCity and high-speed trains. Journal of Sound and Vibration 319, 1036–1066.

Lu, J.F., Jeng, D.S., 2007. A half-space saturated poro-elastic medium subjected to a moving point load. International Journal of Solids and Structures 44, 573–586.

Metrikine, A.V., Verichev, S.N., Blauwendraad, J., 2005. Stability of a two-mass oscillator moving on a beam supported by a visco-elastic half-space. International Journal of Solid and Structures 42, 1187–1207.

Picoux, B., Le Houédec, D., 2005. Diagnosis and prediction of vibration from railway trains. Soil Dynamics and Earthquake Engineering 25, 905–921.

Sheng, X., Jones, C.J.C., 1999. Ground vibration generated by a harmonic load acting on a railway track. Journal of Sound and Vibration 225 (1), 3–28.

Sheng, X., Jones, C.J.C., Thompson, D.J., 2003. A comparison of a theoretical model for quasi-statically and dynamically induced environmental vibration from trains with measurement. Journal of Sound and Vibration 267, 621–635.

Sheng, X., Jones, C.J.C., Thompson, D.J., 2004. A theoretical model for ground vibration from trains generated by the vertical track irregularities. Journal of Sound and Vibration 272, 937–965.

Siddharthan, R., Zafir, Z., Norris, G.M., 1993. Moving load response of layered soil. I: Formulation; II: Verification and application. Journal of Engineering Mechanics, ASCE 119 (10), 2052–2089.

Suiker, A.S.J., Chang, C.S., Borst, R.D., et al., 1999. Surface waves in a stratified half space with enhanced continuum properties. Part 1: Formulation of the boundary value problem. European Journal of Mechanics A: Solids 18, 749–768.

Takemiya, H., Bian, X., 2005. Substructure simulation of inhomogeneous track and layered ground dynamic interaction under train passage. Journal of Engineering Mechanics, ASCE 131 (7), 699–711.

Theodorakopoulos, D.D., 2003. Dynamic analysis of a poroelastic half-plane soil medium under moving loads. Soil Dynamics and Earthquake Engineering 23 (7), 521–533.

Theodorakopoulos, D.D., Chassiakos, A.P., Beskos, D.E., 2004. Dynamic effects of moving load on a poroelastic soil medium by an approximate method. International Journal of Solids and Structures 41 (7), 1801–1822.

Vostroukhov, A.V., Metrikine, A.V., 2003. Periodically supported beam on a visco-elastic layer as a model for dynamic analysis of a high-speed railway track. International Journal of Solids and Structures 40 (21), 5723–5752.

Zai, W., Cai, Z., 1997. Dynamic interaction between a lumped mass vehicle and a discretely supported continuous rail track. Computers and Structures 63 (5), 987–997.

Zai, W., Wang, Q., Chen, D., 1994. A study on the analytical models for wheel/rail dynamics. Journal of the China Railway Society 16 (1), 64–72 (in Chinese).